Long-Range Oxygen Spillover at the Cu/CeO_2 Interface

Boyang Li and Yaqiong Su*

School of Chemistry, Engineering Research Center of Energy Storage Materials and Devices of Ministry of Education, National Innovation Platform (Center) for Industry-Education Integration of Energy Storage Technology, Xi'an Jiaotong University, Xi'an, 710049, China

Corresponding authors: yqsu1989@xjtu.edu.cn (Y. Su)

1. Computational details

1.1 DFT calculations

Computational modeling was carried out using density functional theory (DFT) with the gradient-corrected functional of Perdew, Burke, and Ernzerhof (PBE) as implemented in the CP2K package [1]. The spin-polarized wave functions of Cu and O were expanded with a double-ζ atom-centered Gaussian-type basis to describe the wave functions but used an auxiliary planewave basis to describe the density with 600 Ry energy cutoff [2]. To properly capture the localized 4f electronic states of Ce, the corresponding basis set and pseudoptential were chosen in accordance with established literature[3]. The O 2s, 2p electrons, Cu 3d, 4s electrons, and Ce 4f, 5d, 6s electrons were treated as valence, and the rest were core electrons represented by Goedecker−Teter−Hutter (GTH) pseudopotentials. The dispersion correction was applied in all the calculations with the Grimme-D3 method [4]. In the static DFT calculations, the geometries were optimized by the Broyden−Fletcher−Goldfarb−Shanno (BFGS) minimizer with a force convergence criterion of $4.5e^{-4}$ hartree/bohr. The DFT+U method was utilized in our calculations to describe the Ce 4f electrons. The value of intraatomic coulomb term minus exchange term (U - J) was chosen to be 7.0 eV to reproduce the correct band gap, gap state location, and work function [3]. Reciprocal space mesh consisting of gamma point was used for Brillouin zone integration. The wave function analysis was performed using the Multiwfn software [5, 6]. The adsorption energy of O_2 on the catalyst was calculated according to the following equation:

$$E_{ads} = E_{total} - E_{\text{adsorbate}} - E_{slab}$$

where E_{total}, $E_{adsorbate}$, and E_{slab} are the total energies of adsorbed species on the slab, the adsorbed molecules in the gas phase, and the bare surface, respectively.

1.2 Ab Initio Molecular Dynamics Simulations

AIMD simulations were carried out to investigate the dynamics properties of CeO_2 supported Cu NCs. The calculations started with the DFT-optimized configurations and lattice parameters fixed and were performed for at least 30 ps with a time step of 1 fs. The canonical (NVT) ensemble and Nosé−Hoover thermostats were used with the temperature set to 773 K,

573 K, and 298 K [7, 8].

1.3 Deep Potential Molecular Dynamics

DPMD simulations were carried out using the DeePMD-kit interfaced with LAMMPS package [9]. The machine learning descriptor was constructed from both angular and radial atomic configurations. The embedding network includes 3 layers with neurons in each layer of (25, 50, 100) with 1,000,000 steps of training iteration. The start and limit factors of energy and force were set to 0.02, 1, 1000, and 1, respectively. The cutoff radius for neighbor searching was set to 7.0 Å. The training data set for the deep potential model originated from all the AIMD trajectories mentioned in this study. The accuracy of the DPMD was validated using root-mean-square error (RMSE) and radial distribution function (RDF) analyses. The RMSEs of energy are only ~2.45 meV/atom for Cu/CeO_2 and the RMSEs of forces was ~99 meV/Å for Cu/CeO_2, respectively (**Figure S18**). The RDFs calculated from AIMD and DPMD showed excellent agreement for Cu-Cu, Cu-O, and Ce-O pairs, demonstrating that DPMD can predict local atomic bonding and coordination with DFT-level accuracy (**Figure S19**).

1.4 Computational models

For the model construction, the equilibrium lattice constant (5.49 Å) of CeO_2 bulk was employed [10]. The CeO_2(111) surface periodic slab model was established with a p(6×4) nine-atomic-layer supercell. Additionally, the CeO_2(111) surface model was orthogonalized prior to simulations, facilitating subsequent analysis of dynamic simulations. One 2×4 ceria adlayer was added on a perfect CeO_2(111)-p(6×4) surface to model the step-edges. Typically, the bottom Ce-O-Ce layer was frozen to its bulk position, and the upper two Ce-O-Ce layers and subsequently supported Cu clusters were fully relaxed. To prevent interaction between adjacent units, a vacuum space of 15 Å was utilized. The CeO_2(110) surface was modeled by p(4 × 5) five-atomic-layer supercell, with the bottom two layers fixed. For the CeO_2(100)-O termination, half the O atoms from the outmost layer were moved to the opposing face for surface dipole elimination [11]. The p(5 × 5) consisted of fifteen atomic layers with the bottom three layers fixed in the structural relaxation.

1.5 Data Availability

Computational files and results of simulations as well as the trained model for the analysis have been deposited in Zenodo (https://doi.org/10.5281/zenodo.14616216).

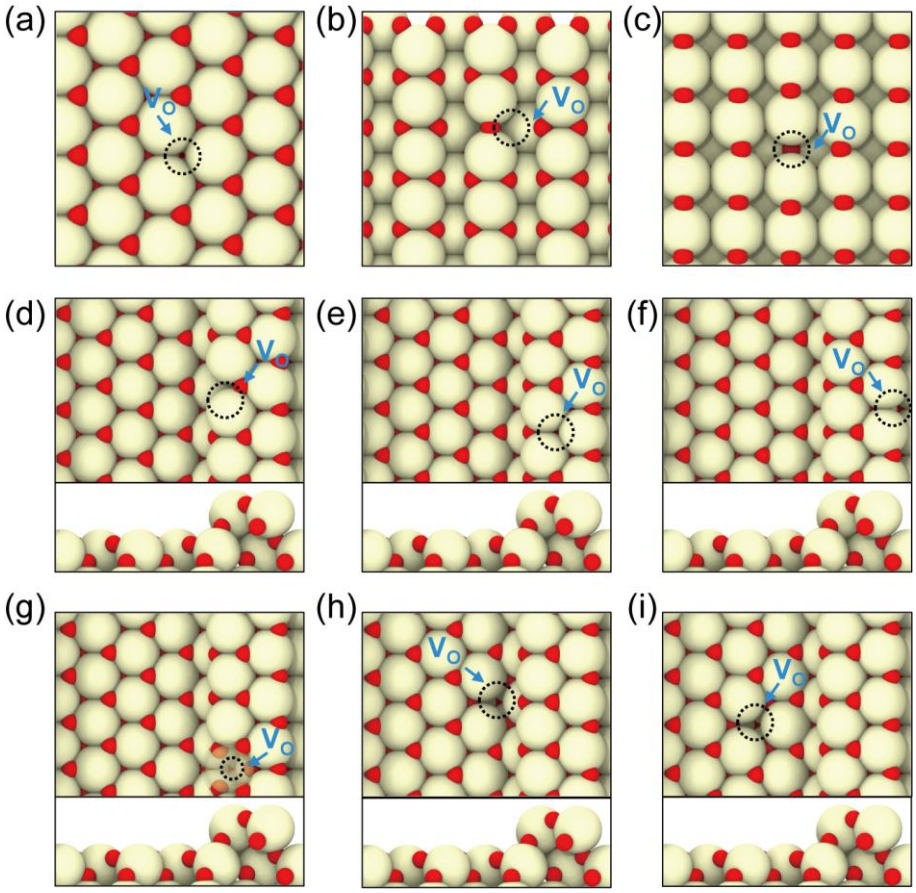

Figure S1. The optimized configuration of different CeO_2 facet with an V_O (a) CeO_2(111); (b) CeO_2(110); (c) CeO_2(100). And the optimized configurations for CeO_2(111)-step with various V_O site. (d) step edges V_O; (e) upper terrace V_O; (f) furthest step edges V_O; (g) V_O underneath the step edge Ce atom; (h) lower terrace V_O near step edge; (i) lower terrace V_O; The black circular dotted line represents the position of the V_O. The color scheme is identical to that used in Figure 1 of the main text. The black circular dotted line represents the position of the V_O. The color scheme is identical to that used in Figure 1 of the main text.

The formation energies of an V_O (E_{V_o}) for different CeO_2 facet were calculated. For the CeO_2(111), the E_{V_o} was found to be 1.93 eV (a), which matches well with the reported literature value of 1.97 eV [3]; Additionally, the E_{V_o} for the CeO_2(110) and CeO_2(100) are determined to be 1.25 eV (b) and 1.42 eV (c), respectively. The E_{V_o} for CeO_2(111)-step at various step sites on the CeO_2(111)-step were further determined. The calculated E_{V_o} were list as below: (d) step edges V_O: 1.50 eV; (e) upper terrace V_O: 1.80 eV; (f) furthest step edges V_O: 1.42 eV; (g) V_O

underneath the step edge Ce atom: 1.71 eV; (h) lower terrace V_O near step edge: 1.83 eV; (i) lower terrace V_O: 1.85 eV;

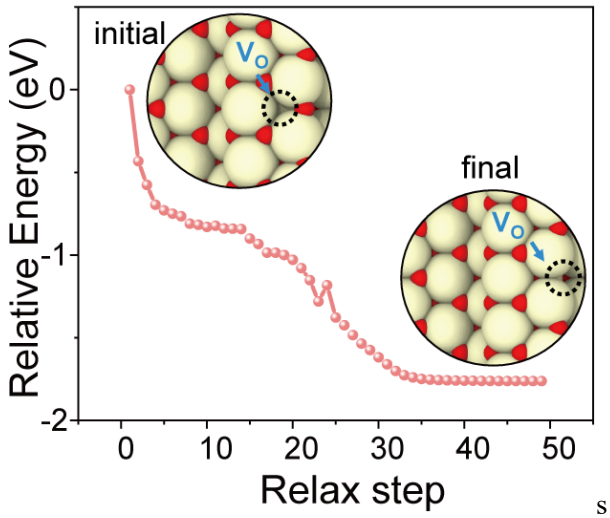

s

Figure S2. Optimization curves of V_O from the subface of the upper terrace to the furthest step edges, along with the optimized structure (inset). The black circular dotted line represents the position of the V_O. The color scheme is identical to that used in Figure 1 of the main text.

When an V_O is added to the subface of the upper terrace on the CeO_2(111)-step, the O atom on the furthest step edges spontaneously spillover to the subface of the upper terrace site during geometry optimization and leading to a more stable configuration. Additionally, the high mobility of oxygen atoms in the CeO_2 lattice facilitates this spontaneous migration, further contributing to the overall stability of the system.

In conclusion, as shown in **Figures S1-2**, the high E_{ads} indicate a strong interaction between Cu and O, which is due to the oxyphilic nature of Cu atoms [12]. These interaction energies are higher than the E_{V_o} on the CeO_2 (110) and (100) surfaces, and slightly lower than on the (111) facet. Additionally, we constructed the CeO_2(111) surface with (110)-type steps (donate as (CeO_2(111)-step)), which is observed in (111) facet experimentally, and determined the E_{V_o} for different lattice O site [13, 14, 15]. The results confirm higher oxygen mobility as expected. These

findings suggest that the high affinity of Cu NCs for O atom, together with the lower E_{V_O} of specific CeO_2 surface.

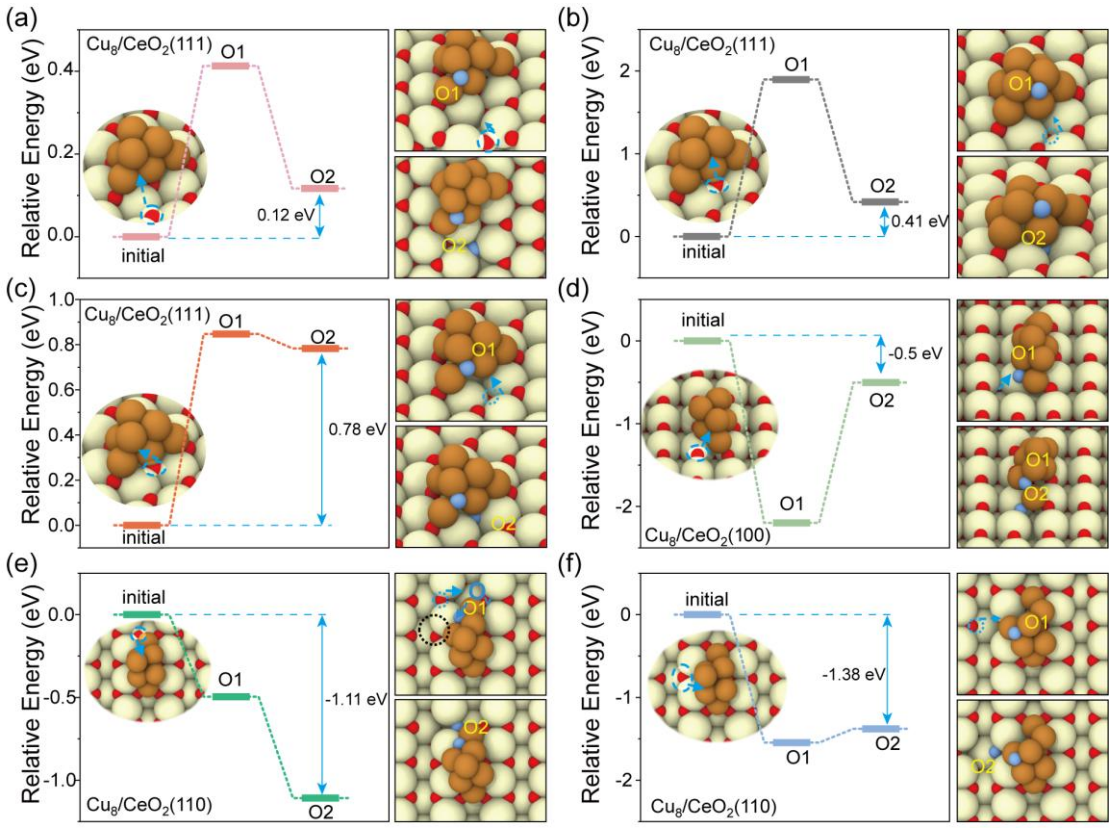

Figure S3. The relative energy and optimization configurations of ROS on the (a-c) $Cu_8/CeO_2(111)$, (d) $Cu_8/CeO_2(100)$, and (e-f) $Cu_8/CeO_2(110)$. The blue circular dotted line represents the readily spillover O atom. The blue atoms represent the spillover O atoms and each of these O atoms has been assigned the indices (O#). The other color scheme is identical to that used in Figure 1 of the main text.

As shown in **Figure S3**, on stoichiometric (111) surfaces, the first terrace lattice O (1O) reverse spillover to the Cu NCs and leaves an V_O, this metastable structure is thermodynamically less stable than the most on CeO_2 (111) by 0.4 eV. And if the vicinity terrace O (2O) migrates to this newly formed V_O, the process becomes exothermic but still results in a configuration less stable by 0.12 eV than the initial state. Additionally, the relative energies for various sites of terrace and sub-terrace O in successive reverse spillover to the Cu NCs were

investigated. In all cases, the final states were less stable compared to configurations without spillover. Additionally, on (110) and (100) surfaces, the spillovers of 1O are thermodynamically favorable processes by -0.5 and -2.2 eV, respectively. Next, the cases of 2O spillover to obtained V_O and adjacent to Cu NCs are energetically more favorable and the obtained Cu_8O_1/CeO_{2-x} are significantly more stable than the original Cu_8/CeO_2.

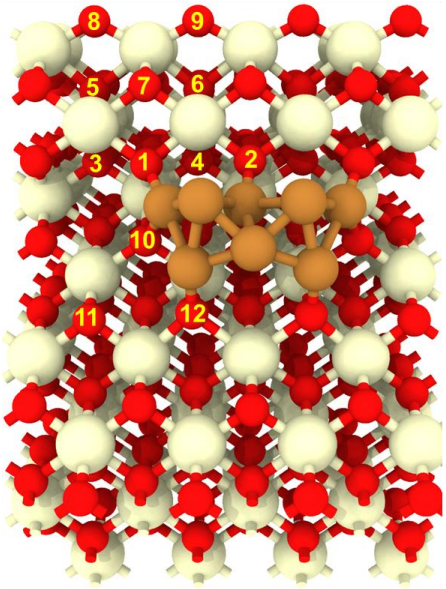

Site	E_{Ov} (eV)
1	2.46
2	2.26
3	2.23
4	2.26
5	1.86
6	1.76
7	2.35
8	1.25
9	1.23
10	2.45
11	2.08
12	3.12

Figure S4. The E_{V_o} of various sites on the Cu_8/CeO_2(111)-step. The color scheme is identical to that used in Figure 1 of the main text.

To further investigate the relative stability of static oxygen spillover at step-edges, the E_{V_o} at various sites on the Cu_8/CeO_2(111)-step was first explored. As shown in **Figure S4**, the E_{V_o} of the Cu-CeO_2 interfacial O increases significantly, while at step-edges, it decreases progressively with the increasing distance from Cu NCs. These results shed light on the potential direction and internal driving force of oxygen spillovers. When an interfacial oxygen atom undergoes reverse spillover to the Cu, the high E_{V_o} at that site drives neighboring lattice oxygen atoms with lower E_{V_o} to spillover and migrate into the resulting vacancy, leading to a more stable configuration.

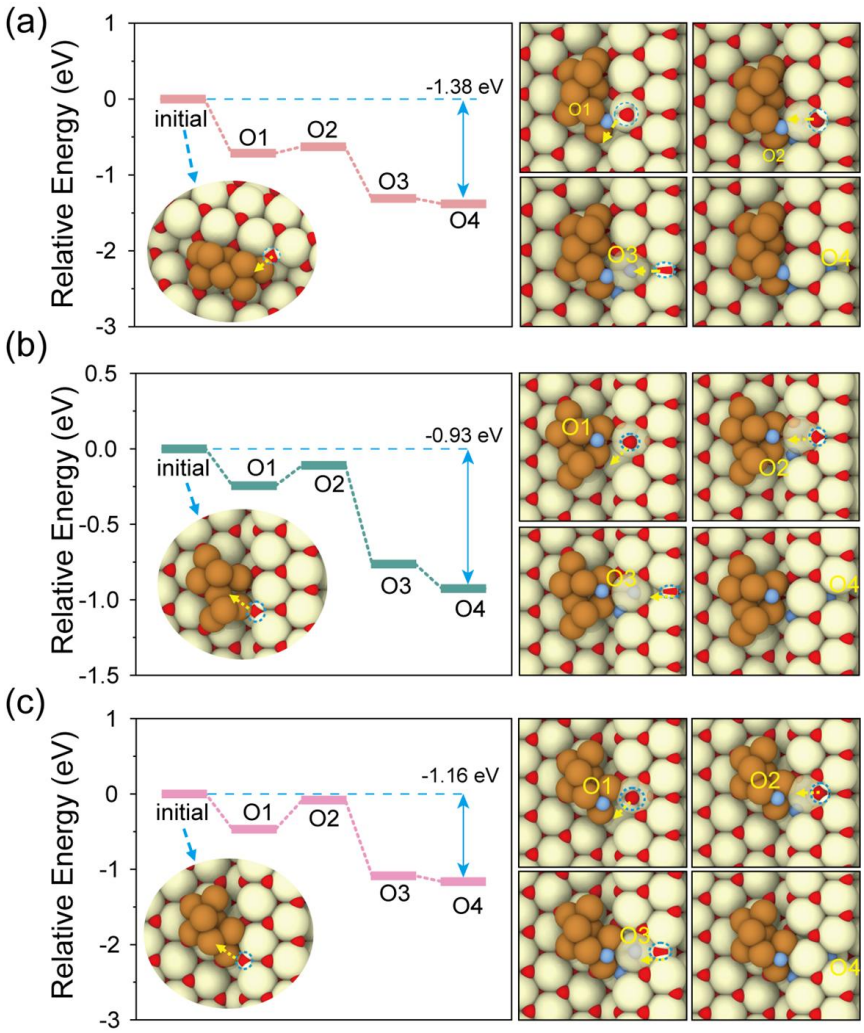

Figure S5. The relative energies and configurations for DFT optimized structures with O spillover in $Cu_8/CeO_2(111)$-step. (a) Comparison of relative energies for ROS starting with one step edge O atom and corresponding configurations; The relative energies and configurations for DFT optimized structures with O spillover in (b) $Cu_8/CeO_2(111)$-step-nd and (c) $Cu_8/CeO_2(111)$-step-rd with various initial Cu NCs configuration.

Based on the hierarchical trend in E_{Vo}, corresponding configurations of oxygen spillover at step edges were constructed and optimized. The structures and the relative energies are presented in **Figure S5a**. The migration of a step-edge oxygen atom (O1) to the Cu cluster is a thermodynamically favorable process, with an energy change of -0.71 eV. If the nearest subsurface step O (O2) subsequently fills the vacancy, the energy of the system slightly

increases by 0.08 eV but is still more stable than the initial by 0.63 eV. However, when a next-nearest subsurface step O (O3) atom migrates to this vacancy, the relative energy decreases significantly with -1 eV. Finally, the transfer of the next-nearest step O (O4) to the newly created vacancy is an exothermic process with an energy change of -0.07 eV. Overall, this final structure is thermodynamically more stable than the initial one by 1.38 eV. Additionally, reverse spillover starting with either two step-edge O atoms (O1-r) or a next-nearest step O (O5) atom was also investigated. These configurations demonstrated increased stability compared to the initial states. The relative energies of these configurations are shown in **Figures S5b-c**. To ensure the reliability and generality of the conclusions on this results, additional Cu NCs with diverse geometries were examined. These configurations, derived from our prior work using machine learning and genetic algorithms, demonstrated consistent behavioral trends despite structural variations. All these results indicate that ROS to Cu NCs, followed by further migration of O atom to the vacancies, can stabilize the supported Cu NCs and create V_O.

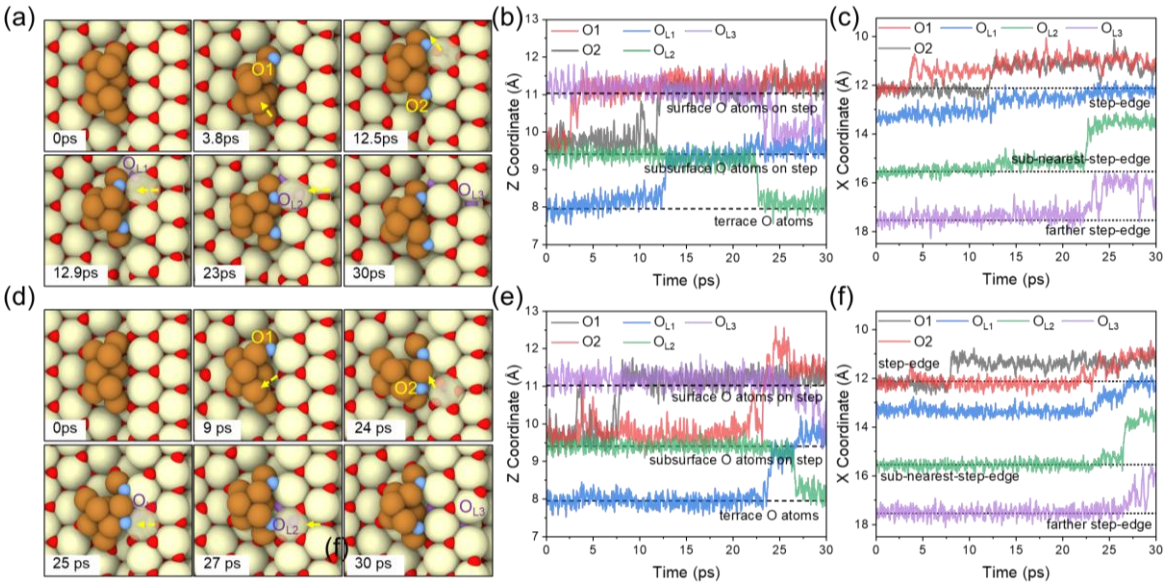

Figure S6. Additional AIMD trajectories of $Cu_8/CeO_2(111)$-step were performed with varied random seeds to assess stochastic variability under identical conditions. (a) Representative snapshots from AIMD (replica 2) at 773 K for $Cu_8/CeO_2(111)$-step; (b) The Z-axis coordinates of ROS O atoms; (c) The X-axis coordinates of ROS O atoms; (d) Representative snapshots

from AIMD (replica 3) at 773 K for Cu_8/CeO_2(111)-step; (e) The Z-axis coordinates of ROS O atoms; (f)The X-axis coordinates of ROS O atoms; The color scheme is identical to that used in Figure 2 of the main text.

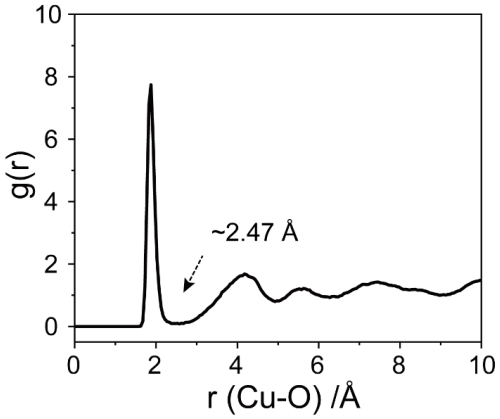

Figure S7. The RDF of Cu-O atom pair in the AIMD of Cu_8/CeO_2-step at 773K.

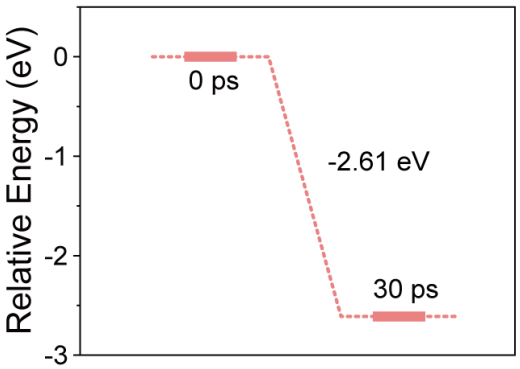

Figure S8. The DFT optimized relative energy of initial and final configuration after 30 ps AIMD at 773K for Cu_8/CeO_2-step.

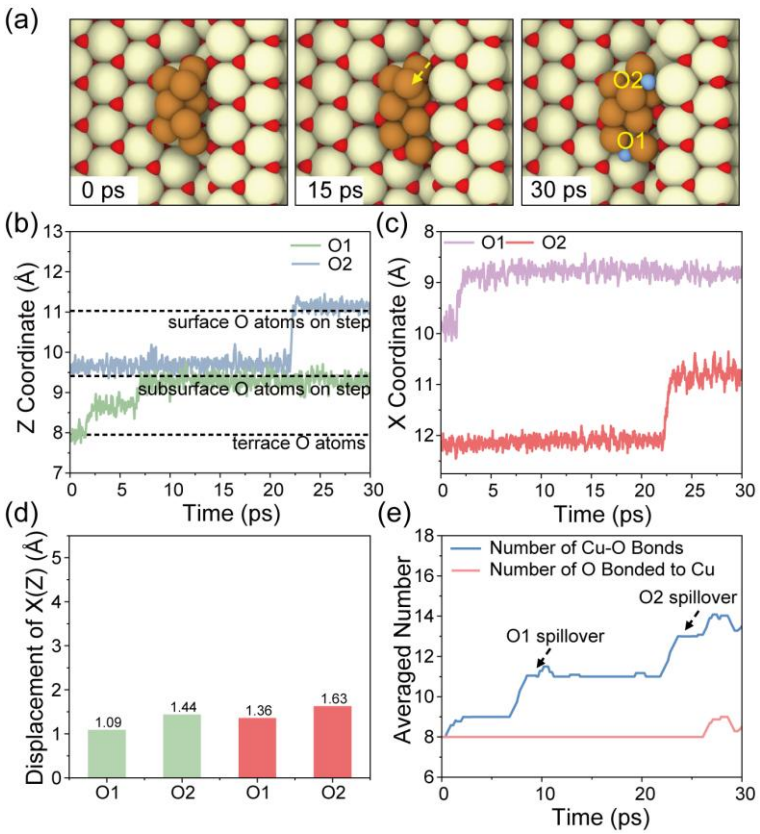

Figure S9. ROS takes place in the AIMD simulation at 298 K for the $Cu_8/CeO_2(111)$-step. (a) Typical snapshots in AIMD. The color scheme is identical to that used in Figure 2 of the main text; (b) The Z-axis coordinates of ROS O atoms in AIMD; (c) The X-axis coordinates of ROS O atoms in AIMD; (d) The displacement of X coordinates (green) and Z coordinates (red) for ROS O after 30 ps; (e) The number of Cu–O bonds (blue line) and the total O atoms bonded to Cu_8 (red line). The numbers on both curves are also averaged by the data of the following 0.5 ps;

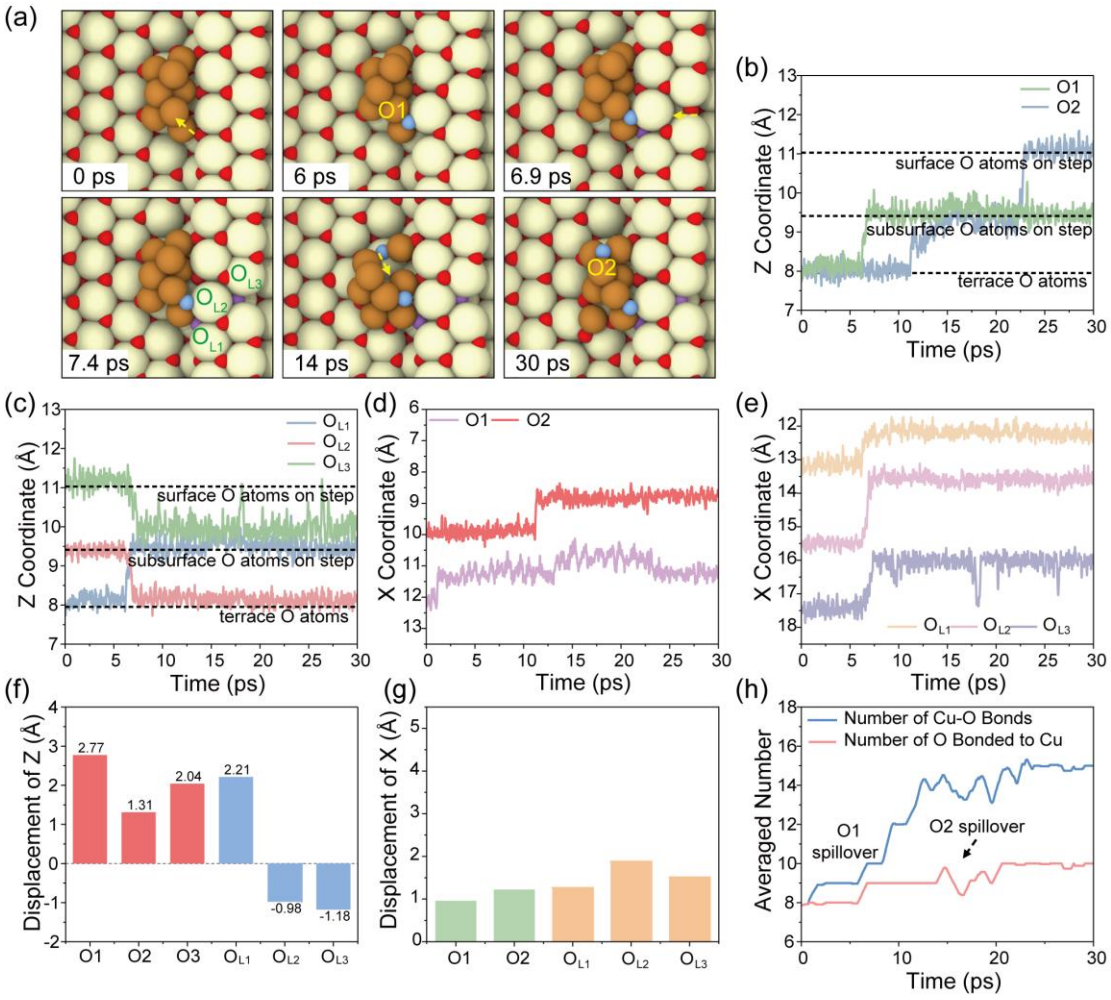

Figure S10. ROS takes place in the AIMD simulation at 573 K for the $Cu_8/CeO_2(111)$-step. (a) Typical snapshots in AIMD. The color scheme is identical to that used in Figure 2 of the main text; (b-c) The Z-axis coordinates of ROS O atoms in AIMD; (d-e) The X-axis coordinates of ROS O atoms in AIMD; (f) The displacement of Z coordinates for ROS O after 30 ps; (g) The displacement of X coordinates for ROS O after 30 ps; (h) The number of Cu–O bonds (blue line) and the total O atoms bonded to Cu_8 (red line). The numbers on both curves are also averaged by the data of the following 0.5 ps;

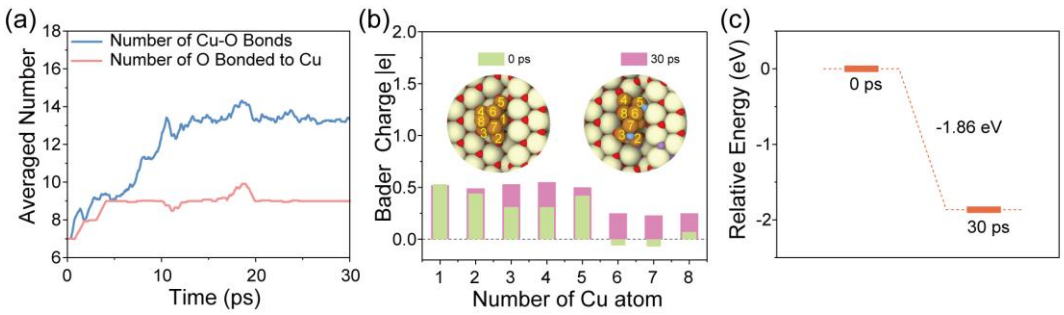

Figure S11. ROS takes place in the AIMD simulation for the $Cu_8/CeO_2(111)$-step-V_O. (a) The number of Cu–O bonds (blue line) and the total O atoms bonded to Cu_8 (red line). The numbers on both curves are also averaged by the data of the following 0.5 ps; (b) the Bader charge of Cu atoms before and after 30 ps AIMD for Cu_8/CeO_2-step-V_O; (c) the DFT optimized relative energy of initial and final configuration after 30 ps AIMD at 773K for $Cu_8/CeO_2(111)$-step-V_O.

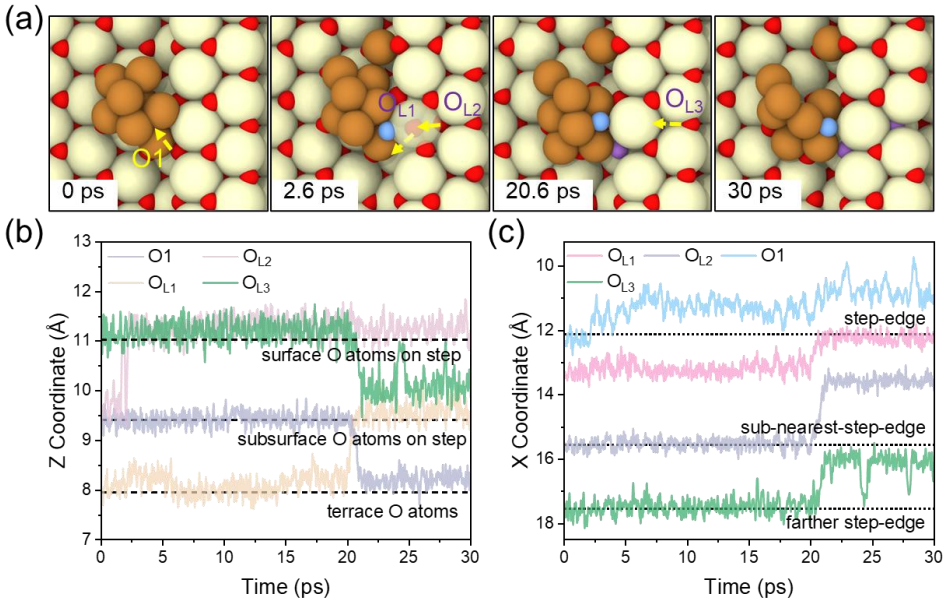

Figure S12. AIMD trajectories of $Cu_8/CeO_2(111)$-step were performed with varied initial Cu NC structure. (a) Representative snapshots from AIMD (replica 2) at 773 K; (b) The Z-axis coordinates of ROS O atoms; (c) The X-axis coordinates of ROS O atoms; The color scheme is identical to that used in Figure 2 of the main text.

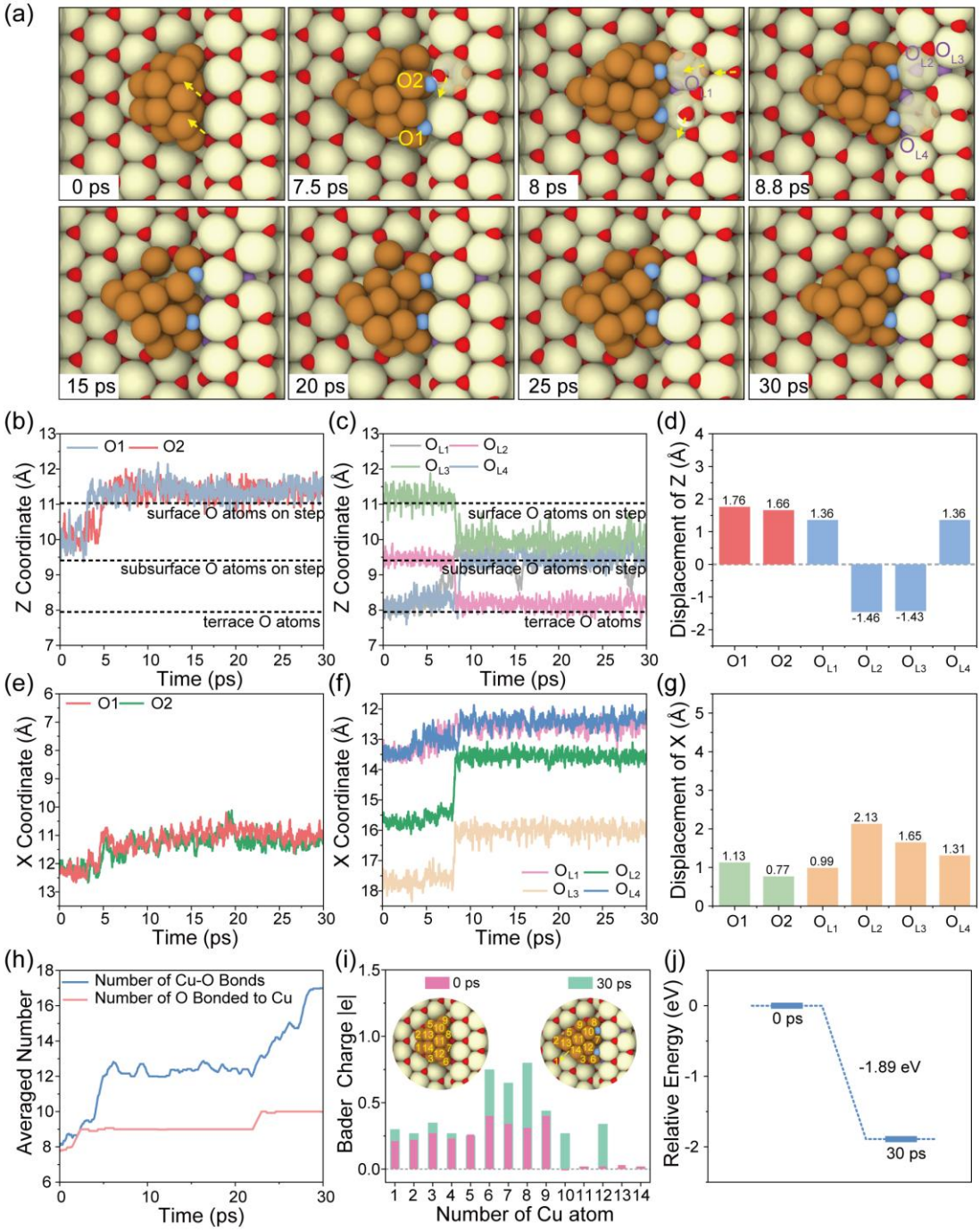

Figure S13. ROS place in the AIMD simulation for the $Cu_{14}/CeO_2(111)$-step. The optimized configuration of $Cu_{14}/CeO_2(111)$-step was shown as 0ps. (a) Typical snapshots in AIMD of 30 ps at 773 K; The color scheme is identical to that used in Figure 2 of the main text; (b-c) The Z-axis coordinates of ROS O atoms in AIMD; (d) The displacement of Z coordinates for ROS O after 30 ps; (e-f) The X-axis coordinates of ROS O atoms in AIMD; (g) The displacement of X coordinates for ROS O after 30 ps; (h) The number of Cu–O bonds (blue line) and the total O atoms bonded to Cu_8 (red line). The numbers on both curves are also

averaged by the data of the following 0.5 ps; (i) the Bader charge of Cu atoms before and after 30 ps AIMD; (j) the DFT optimized relative energy of initial and final configuration after 30 ps AIMD.

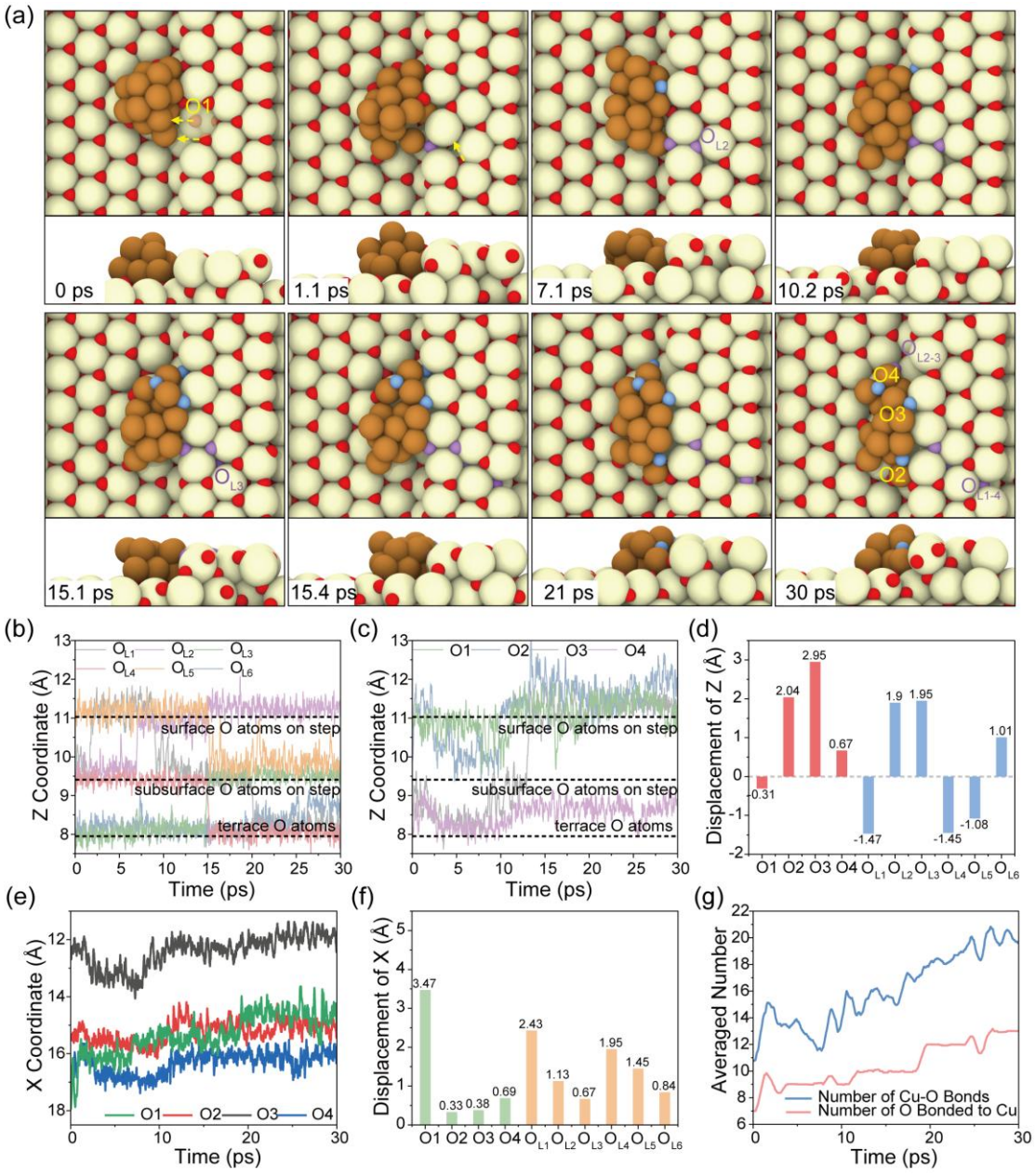

Figure S14. ROS takes place in the AIMD simulation for the $Cu_{14}/CeO_2(111)$-3step-V_O. (a) Typical snapshots in AIMD of 30 ps at 773 K. The color scheme is identical to that used in Figure 2 of the main text; (b-c) The Z-axis coordinates of ROS O atoms in AIMD; (d) The

displacement of Z coordinates for ROS O after 30 ps; (e) The X-axis coordinates of ROS O atoms in AIMD; (f) The displacement of X coordinates for ROS O after 30 ps; (g) The number of Cu–O bonds (blue line) and the total O atoms bonded to Cu_8 (red line). The numbers on both curves are also averaged by the data of the following 0.5 ps.

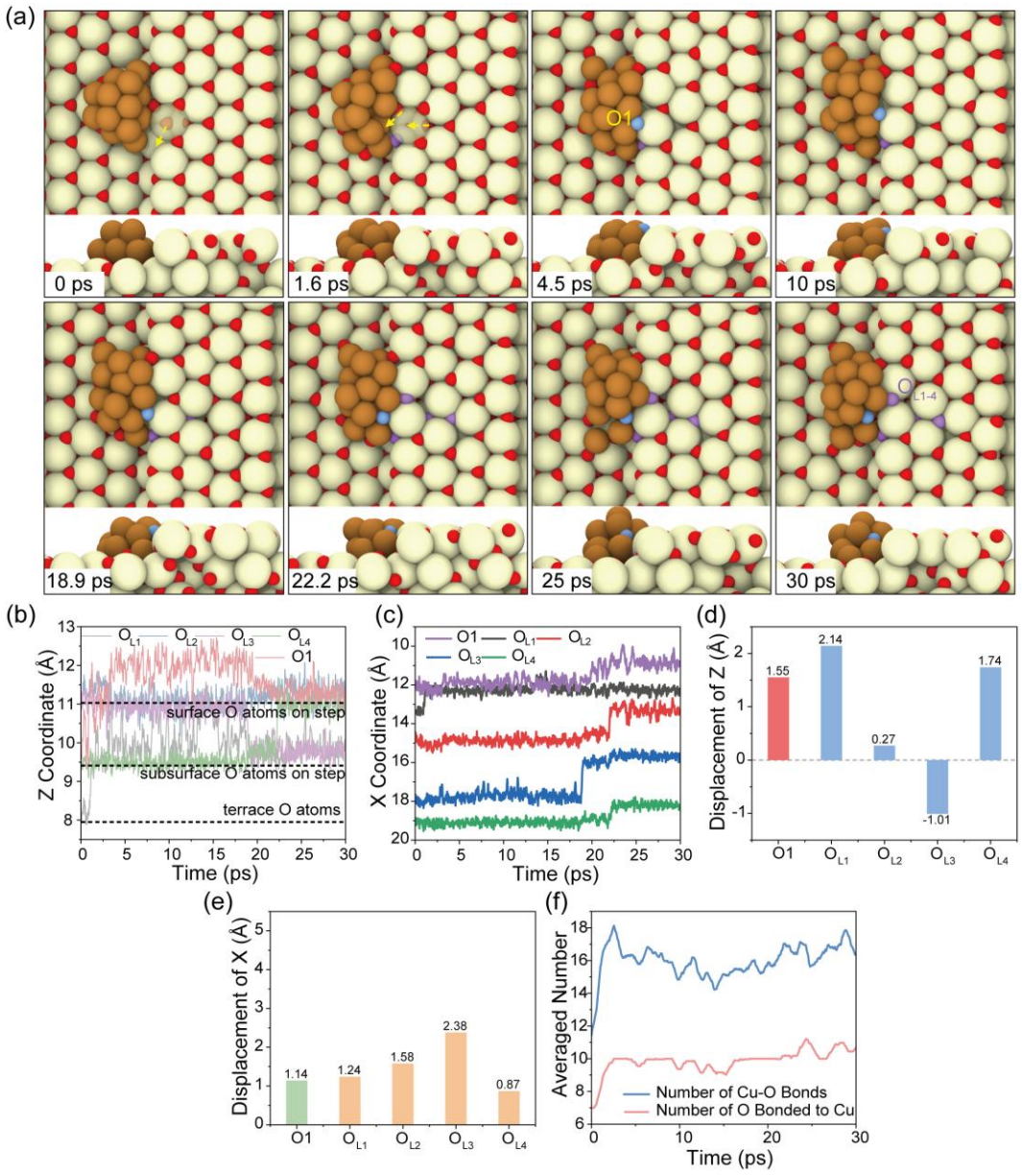

Figure S15. ROS takes place in the AIMD simulation for the $Cu_{14}/CeO_2(111)$-4step-V_O. (a) Typical snapshots in AIMD of 30 ps at 773 K. The color scheme is identical to that used in Figure 2 of the main text; (b) The Z-axis coordinates of ROS O atoms in AIMD; (c) The X-axis coordinates of ROS O atoms in AIMD; (d) The displacement of Z coordinates for ROS O after

30 ps; (e) The X-axis coordinates of ROS O atoms in AIMD; (f) The number of Cu–O bonds (blue line) and the total O atoms bonded to Cu_8 (red line). The numbers on both curves are also averaged by the data of the following 0.5 ps.

In addition, dynamic simulations were performed on systems with various initial Cu NCs to further explore their ROS behavior (**Figures S12**). The size effects of Cu NCs on ROS was considered by employing the larger Cu NCs as candidates ($Cu_{14}/CeO_2(111)$-step, **Figures S13**). For the $Cu_{14}/CeO_2(111)$-step, simulation at 773K revealed a slightly earlier ROS process (approximately 3ps) compared with smaller Cu NCs counterparts. Additionally, the size effects of step-edges monolayers are also considered. **Figures S14-15** illustrate both models exhibited the ROS phenomena with a rapid initiation time. The maximum spillover range are 3.47 Å for $Cu_{14}/CeO_2(111)$-3step-O_v and 2.38 Å for $Cu_{14}/CeO_2(111)$-4step-V_O, confirming the long-range ROS. Consequently, structures with V_O exhibited accelerated ROS initiation compared to non-O_v configurations, which is attributed to the enhanced mobility of oxygen atoms.

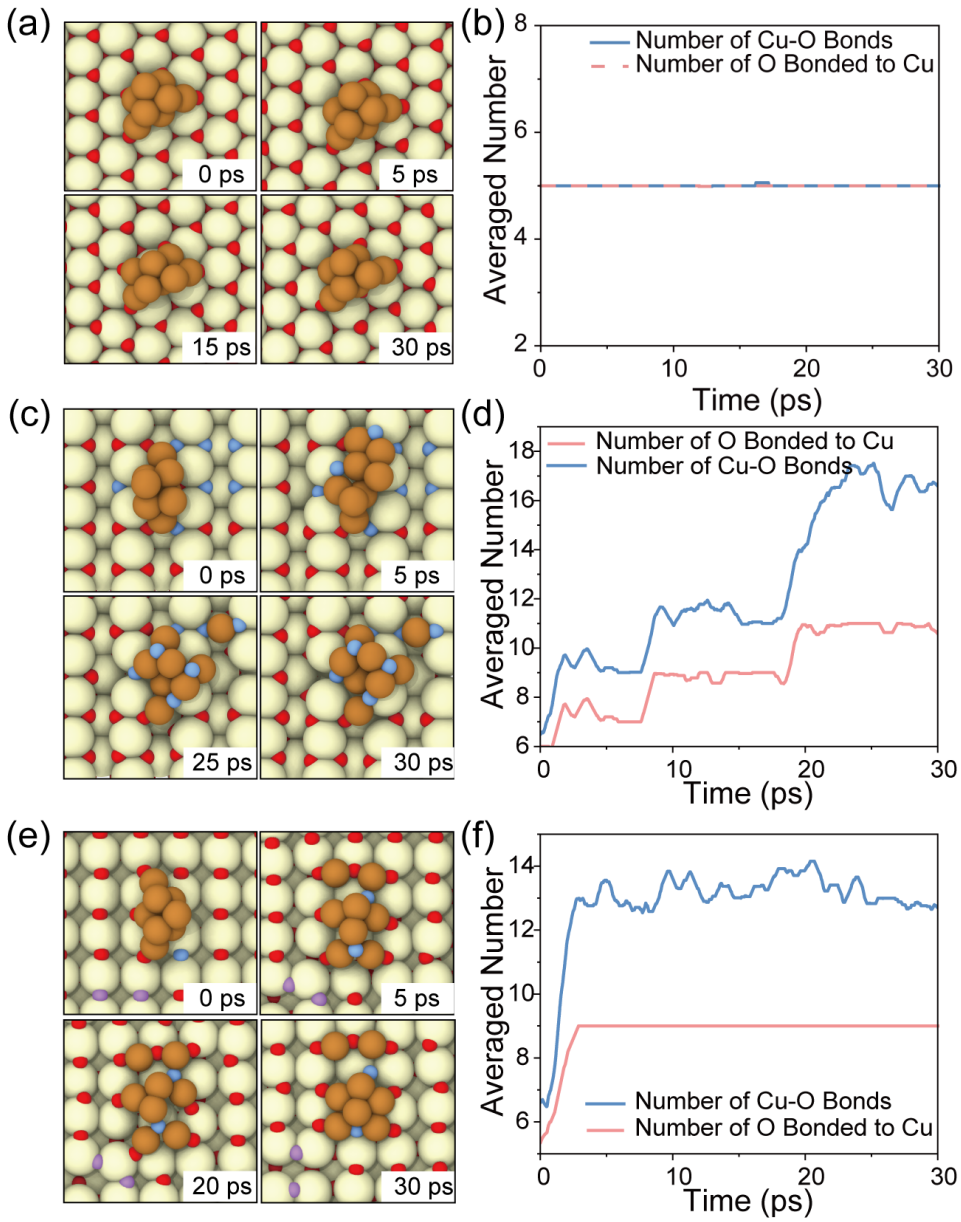

Figure S16. (a) The AIMD snapshots at 773 K for $Cu_8/CeO_2(111)$; (b) The average number of Cu-O bonds and O atoms bonded on Cu NCs; (c) The AIMD snapshots at 773 K for $Cu_8/CeO_2(110)$; (d) The average number of Cu-O bonds and O atoms bonded on Cu NCs; (e) The AIMD snapshots at 773 K for $Cu_8/CeO_2(100)$; (f) The average number of Cu-O bonds and O atoms bonded on Cu NCs; The numbers on both curves are averaged by the data of the following 0.5 ps. The color scheme is identical to that used in Figure 2 of the main text.

The AIMD simulations were conducted for bilayer Cu_8 nanoclusters (NCs) anchored on

stoichiometric CeO_2(111) surfaces to explore ROS behavior. As shown in **Figure S16a**, the bilayer configuration remained stable throughout the 30 ps AIMD simulation at 773 K. The relatively constant average number of Cu-O bonds and O atoms bonded on Cu NCs (**Figure S16b**) also provide evidence which Cu structure is stabilized on CeO_2(111) by coordinating with five O atoms, without the occurrence of ROS during the current timescale. In contrast, the CeO_2(100) facet exhibited significant structural rearrangements of the Cu nanoclusters within the first 5 ps, leading to increased Cu–O coordination and enhanced charge transfer between Cu and CeO_2. For the CeO_2(110) facet (**Figure S16c**), the Cu–O bonds and oxygen coordination gradually increased with ROS progression, eventually reaching levels comparable to the CeO_2(100) facet.

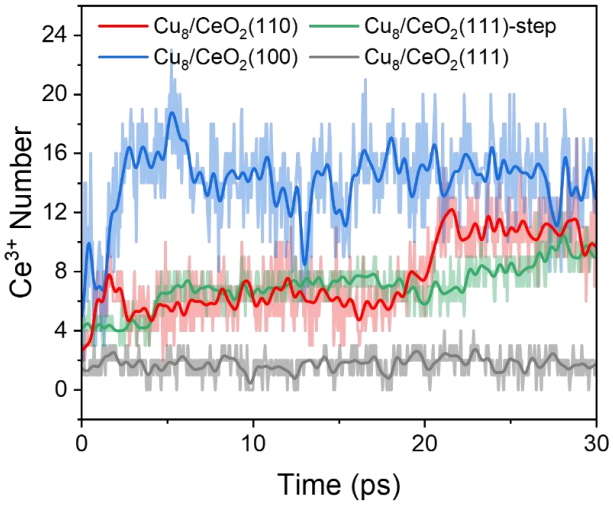

Figure S17. The number of Ce^{3+} during the AIMD simulations at 773 K for Cu_8/CeO_2(110), Cu_8/CeO_2(100), Cu_8/CeO_2(111), and Cu_8/CeO_2(111)-step; The data for both curves have been smoothed for clarity.

To further investigate the dynamic ROS mechanism, we analyzed the evolution of Ce^{3+} concentrations on the various CeO_2 facets over the simulation time (**Figures S17**). On the CeO_2(111) facet, the Ce^{3+} concentration remained constant throughout the AIMD simulation,

attributed to the absence of ROS and the structural stability of the Cu_8 NCs. In the CeO_2(100), the high dispersion of Cu atoms further facilitated Ce^{3+} formation, resulting in a sharp increase that stabilized over time. For the CeO_2(110) facet, the Ce^{3+} concentration gradually increased with ROS progression, correlating with a rise in Cu–O bonds and oxygen coordination. On the Cu_8/ CeO_2(111)-step structure, the Ce^{3+} concentration also increased during ROS, but the extent of the increase and final concentration were lower than those of the CeO_2(100) and (110) facets.

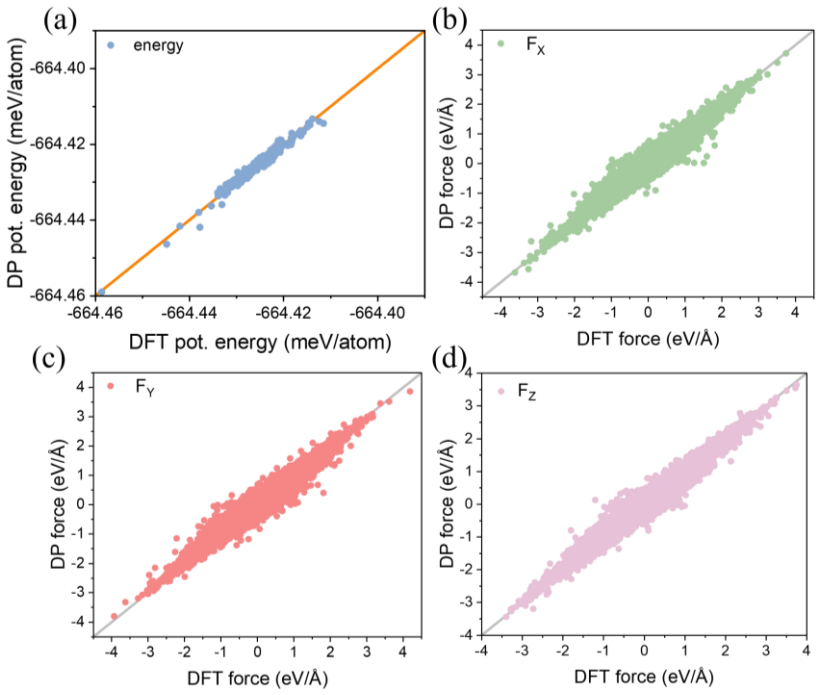

Figure S18. Comparison between DFT and Deep Potential. Comparison of energies and forces for Cu/CeO_2, and corresponding root mean square error of energy (rmse_e) and force (rmse_f). Horizontal and vertical axes represent the energy and forces calculated by CP2K and predicted by DeePMD-kit, respectively.

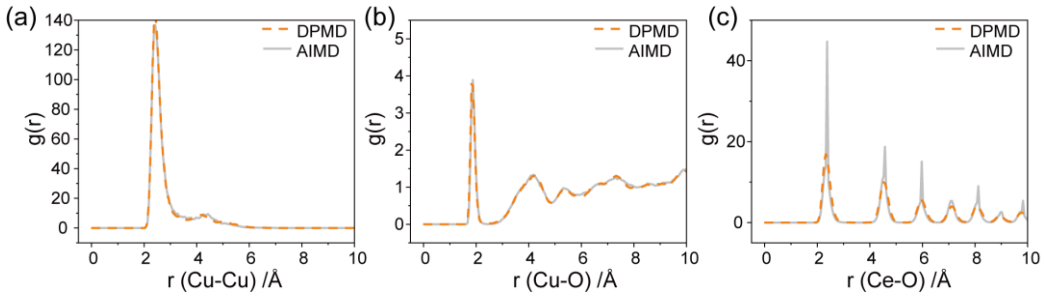

Figure S19. Radius distribution functions (RDFs). RDF of (a) Cu-Cu, (b) Cu-O, and (c) Ce-O for Cu_8/CeO_2 from AIMD and DPMD simulations at 773 K.

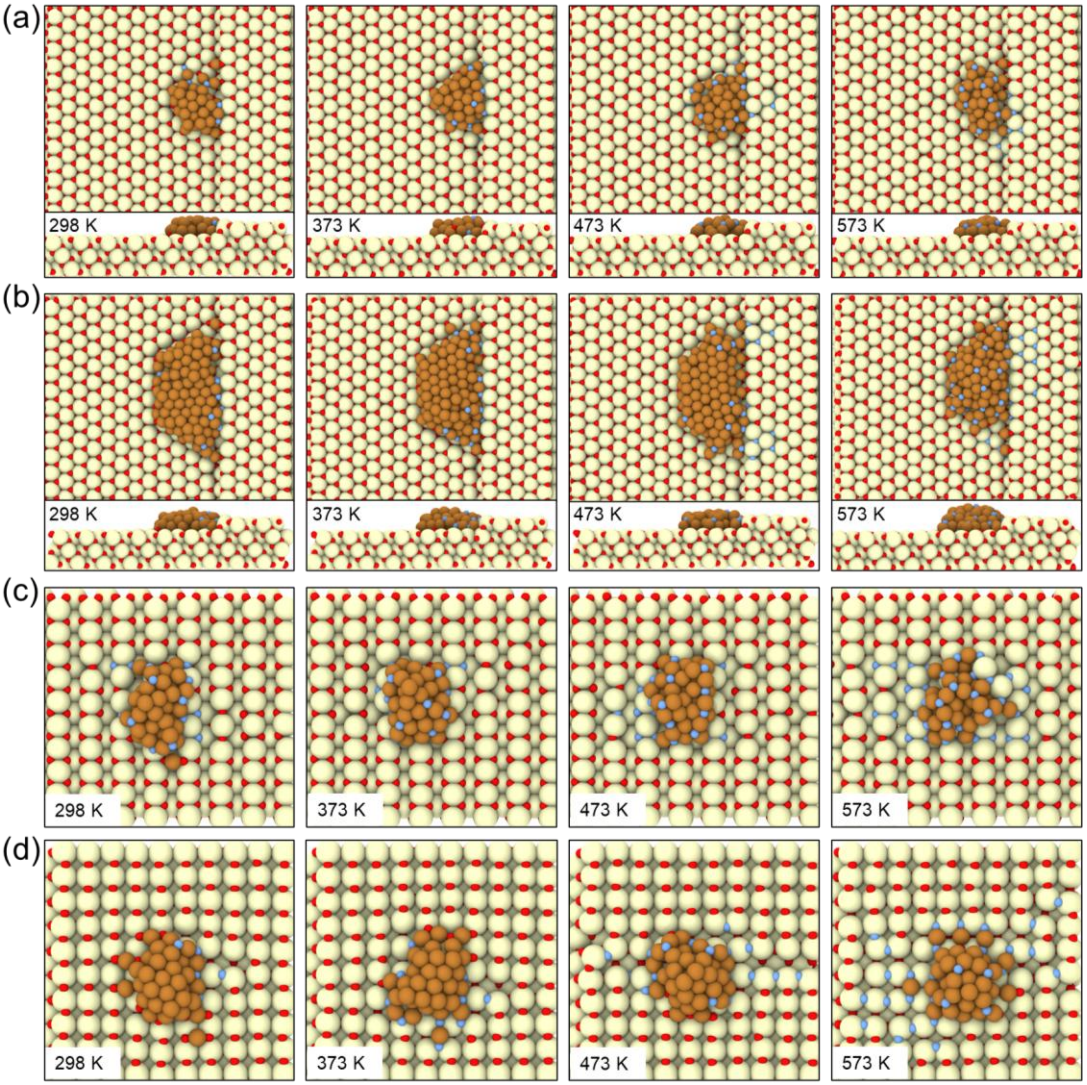

Figure S20. DPMD simulations of 1000ps snapshots for (a) Cu_{37}/CeO_2-step, (b) Cu_{128}/CeO_2-step, (e) Cu_{37}/CeO_2(110), and (d) Cu_{37}/CeO_2(100) at 298K, 373K, 473K, and 573K.

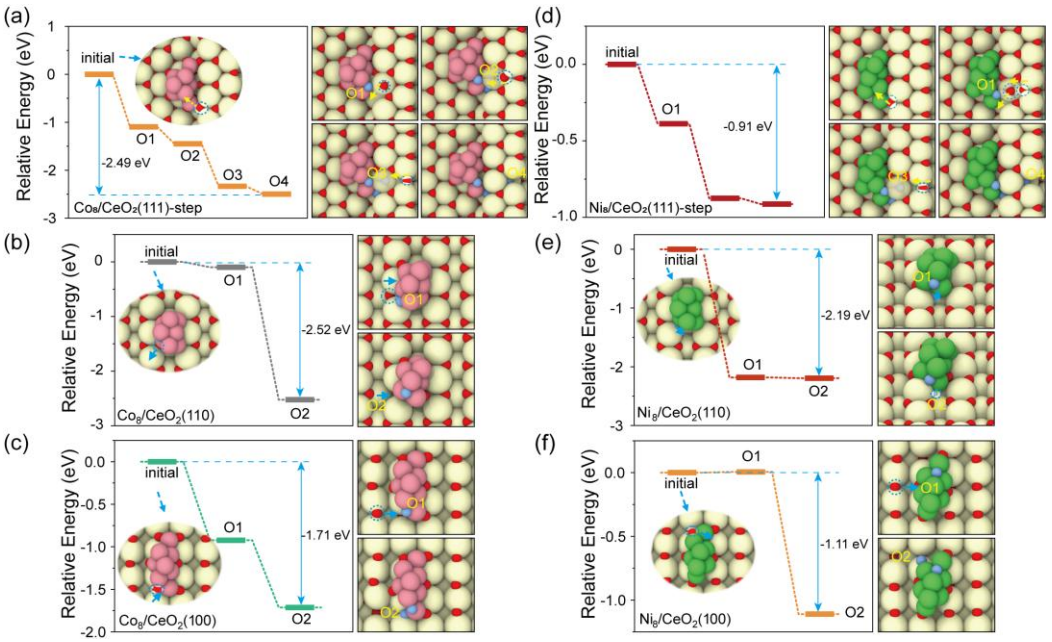

Figure S21. The relative energy and optimization configurations of ROS on the $Co_8/CeO_2$and Ni_8/CeO_2. The blue circular dotted line represents the spillover O atom. Color code: pink (Co) and others is identical to that used in Figure 1 of the main text. The relative energy and optimization configurations of ROS on the (a) $Co_8/CeO_2(100)$; (b) $Co_8/CeO_2(110)$; (c) $Co_8/CeO_2(111)$-step; (d) $Ni_8/CeO_2(111)$-step; (e) $Ni_8/CeO_2(110)$; (f) $Ni_8/CeO_2(100)$.

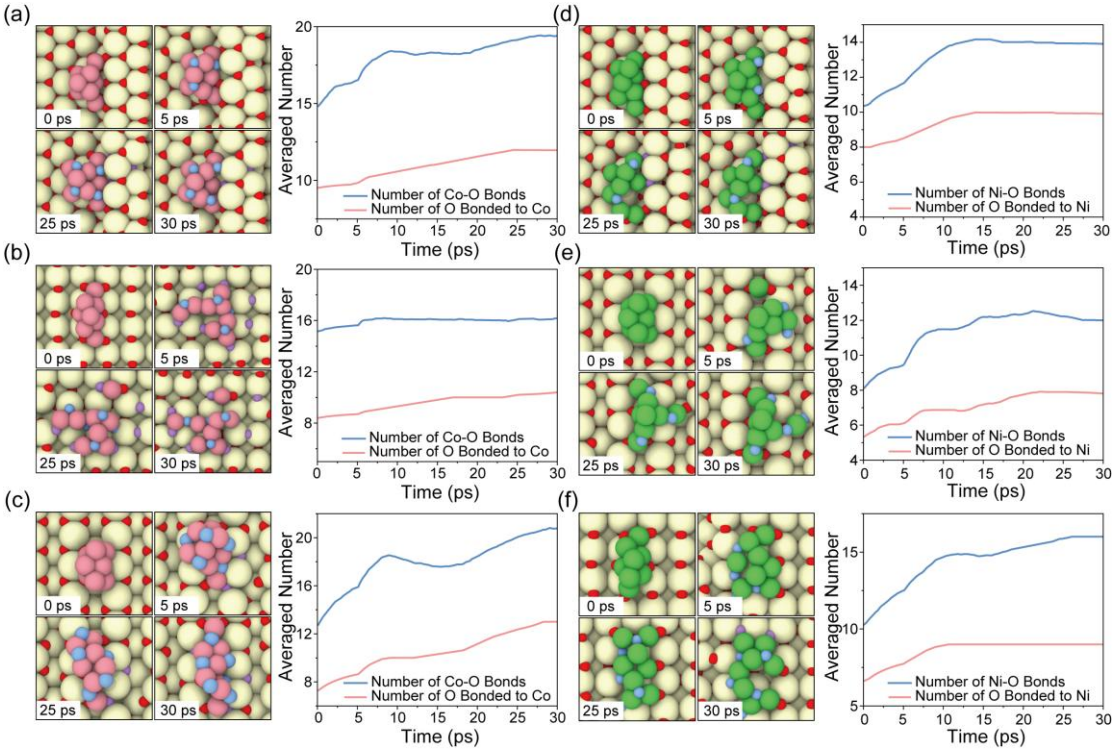

Figure S22. The DPMD snapshots at 773 K for Co_8/CeO_2 and Ni_8/CeO_2 and corresponding average number of Co-O bonds and O atoms bonded on Co NCs: (a) Co_8/CeO_2(111)-step; (b) Co_8/CeO_2(100); (c) Co_8/CeO_2(110); (d) Ni_8/CeO_2(111)-step; (e) Ni_8/CeO_2(110); (f) Ni_8/CeO_2(100); The numbers on both curves are averaged by the data of the following 0.5 ps. Color code: pink (Co), green (Ni), and others is identical to that used in Figure 2 of the main text.

To extend the scope of our study, we systematically investigated the ROS behavior of Ni and Co on various CeO_2 facets through a combination of static DFT calculations and dynamic simulations (**Figure S21-22**). The results reveal that both Ni and Co exhibit ROS dynamics similar to those observed for Cu, with a clear dependence on the CeO_2 facet. These findings suggest that the ROS mechanism is not unique to Cu but is potentially generalizable to other transition metals with comparable properties. This expands the applicability of our conclusions and aligns well with reported literature [16, 17].

References

[1] T. D. Kühne, M. Iannuzzi, M. Del Ben, V. V. Rybkin, P. Seewald, F. Stein, T. Laino, R. Z. Khaliullin, O. Schütt, F. Schiffmann, D. Golze, J. Wilhelm, S. Chulkov, M. H. Bani-Hashemian, V. Weber, U. Borštnik, M. Taillefumier, A. S. Jakobovits, A. Lazzaro, H. Pabst, T. Müller, R. Schade, M. Guidon, S. Andermatt, N. Holmberg, G. K. Schenter, A. Hehn, A. Bussy, F. Belleflamme, G. Tabacchi, A. Glöß, M. Lass, I. Bethune, C. J. Mundy, C. Plessl, M. Watkins, J. VandeVondele, M. Krack, J. Hutter, *J. Chem. Phys.* **2020**, *152*, 194103.

[2] J. Enkovaara, C. Rostgaard, J. J. Mortensen, J. Chen, M. Dułak, L. Ferrighi, J. Gavnholt, C. Glinsvad, V. Haikola, H. A. Hansen, H. H. Kristoffersen, M. Kuisma, A. H. Larsen, L. Lehtovaara, M. Ljungberg, O. Lopez-Acevedo, P. G. Moses, J. Ojanen, T. Olsen, V. Petzold, N. A. Romero, J. Stausholm-Møller, M. Strange, G. A. Tritsaris, M. Vanin, M. Walter, B. Hammer, H. Häkkinen, G. K. H. Madsen, R. M. Nieminen, J. K. Nørskov, M. Puska, T. T. Rantala, J. Schiøtz, K. S. Thygesen, K. W. Jacobsen, *J. Phys. Condens. Matter.* **2010**, *22*, 253202.

[3] Y.-G. Wang, D. Mei, J. Li, R. Rousseau, *J. Phys. Chem. C* **2013**, *117*, 23082-23089.

[4] S. Grimme, J. Antony, S. Ehrlich, H. Krieg, *J. Chem. Phys.* **2010**, *132*, 154104.

[5] T. Lu, F. Chen, *J. Comput. Chem.* **2012**, *33*, 580-592.

[6] T. Lu, *J. Chem. Phys.* **2024**, *161*, 082503.

[7] S. Nosé, *J. Chem. Phys.* **1984**, *81*, 511-519.

[8] W. G. Hoover, *Phys.Rev.A* **1985**, *31*, 1695-1697.

[9] H. Wang, L. Zhang, J. Han, W. E, *Comput. Phys. Commun.* **2018**, *228*, 178-184.

[10] J. L. F. Da Silva, M. V. Ganduglia-Pirovano, J. Sauer, V. Bayer, G. Kresse, *Phys.Rev.B* **2007**, *75*, 045121

[11] Y. Chen, Q. Wan, L. Cao, Z. Gao, J. Lin, L. Li, X. Pan, S. Lin, X. Wang, T. Zhang, *J. Catal.* **2022**, *415*, 174-185.

[12] Q. Wan, F. Wei, Y. Wang, F. Wang, L. Zhou, S. Lin, D. Xie, H. Guo, *Nanoscale* **2018**, *10*, 17893-17901.

[13] S. Torbrügge, M. Cranney, M. Reichling, *Appl. Phys. Lett.* **2008**, *93*, 073112.

[14] N. Nilius, S. M. Kozlov, J.-F. Jerratsch, M. Baron, X. Shao, F. Viñes, S. Shaikhutdinov, K. M. Neyman, H.-J. Freund, *ACS Nano* **2012**, *6*, 1126-1133.

[15] H. Y. Kim, G. Henkelman, *J. Phys. Chem. Lett.* **2013**, *4*, 216-221.

[16] C.-X. Wang, L.-Y. Zhang, W.-W. Wang, F. Yang, C.-J. Jia, *ACS Catal.* **2024**, *14*, 9421-9430.

[17] A. Parastaev, V. Muravev, E. Huertas Osta, A. J. F. van Hoof, T. F. Kimpel, N. Kosinov, E. J. M. Hensen, *Nat. Catal.* **2020**, *3*, 526-533.